Supporting Information (SI)

3D Acceptors with Multiple A-D-A Architectures for Highly Efficient Organic Solar Cells

Hongbin Chen[†,[a]], Zhe Zhang[†,[a]], Peiran Wang[[a]], Yunxin Zhang[[b]], Kangqiao Ma[[a]], Yi Lin[[c]], Tainan Duan[[d]], Tengfei He[[b]], Zaifei Ma[[c]], Guankui Long[[b]], Chenxi Li[[a]], Bin Kan*[[b]], Zhaoyang Yao*[[a]], Xiangjian Wan[[a]], Yongsheng Chen*[,[a]]

[a]State Key Laboratory and Institute of Elemento-Organic Chemistry, The Centre of Nanoscale Science and Technology and Key Laboratory of Functional Polymer Materials, Renewable Energy Conversion and Storage Center (RECAST), College of Chemistry, Nankai University, Tianjin 300071, China.

[b]School of Materials Science and Engineering, National Institute for Advanced Materials, Renewable Energy Conversion and Storage Center (RECAST), Nankai University, 300350, Tianjin, China.

[c]State Key Laboratory for Modification of Chemical Fibers and Polymer Materials, Center for Advanced Low-dimension Materials, College of Materials Science and Engineering, Donghua University, Shanghai 201620, China.

[d]Chongqing Institute of Green and Intelligent Technology, Chongqing School, University of Chinese Academy of Sciences (UCAS Chongqing), Chinese Academy of Sciences

[†]These authors contributed equally: Hongbin Chen, Zhe Zhang.
Corresponding E-mails: yschen99@nankai.edu.cn (Y.C.); zyao@nankai.edu.cn (Z.Y.); kanbin04@nankai.edu.cn (B.K).

Contents

1. Materials and Methods

2. Synthesis of CH8-0, CH8-1 and CH8-2

3. Figures and Tables

4. References

1. Materials and Methods.

Materials.

Polymeric donor PM6 and the ending unit INCN-2F were purchased from Organtec.Ltd and Woerjiming (Beijing) Technology Development Institute, respectively. Starting material 1-1 and 1-2 were synthesized according to our previously reported method.[1] All the other reagents and chemicals were purchased from commercial suppliers and used directly without further purification unless otherwise noted. The overall synthetic route and detailed synthesized procedures of CH8-0, CH8-1 and CH8-2 and the corresponding characterizations were displayed in "Synthesis of CH8-0, CH8-1 and CH8-2" below.

Methods.

Computational methods in this work. All alkyl chains were replaced with methyl groups (-CH_3) to reduce the computational requirements. The structures were subsequently optimized with Density Functional Theory (DFT) in vacuum within the Gaussian 16 software.[2] The structure optimization, frequency analysis, energy level of frontier molecular orbital and electron reorganization energy were obtained at the Becke three-parameter Lee-Yang-Parr (B3LYP)[3] hybrid functional with the 6-31G(d) basis set.[4] Following equation was used in evaluating electron reorganization energy (λ), $\lambda = [E_2 - E_3] + [E_4 - E_1]$; Here, E_1/E_3 are the energies of the optimized neutral/anion structures of molecule, respectively; E_2/E_4 represent the single point energies of getting/losing an electron for a molecule at the neutral/anion optimized configuration, respectively.

UV–visible (UV-*Vis*) absorption. UV-*Vis* spectra were obtained by a Cary 5000 UV-*Vis* spectrophotometer. The diluted solutions of CH8-0, CH8-1 and CH8-2 were kept at a low concentration of 10^{-5} M.

Thermogravimetric (TGA) analysis. The TGA was carried out on a NETZSCH STA 409PC instrument under purified nitrogen gas flow. The heating rate is a 10 °C min^{-1}.

Cyclic voltammetry (CV). The CV experiments of CH8-0, CH8-1 and CH8-2 were performed with a LK98B II Microcomputer-based Electrochemical Analyzer. All measurements were conducted at room temperature with a three-electrode configuration, including a glassy carbon electrode as the working electrode, a saturated calomel electrode (SCE) as the reference electrode, and a Pt wire as the counter electrode. Tetrabutyl ammonium phosphorus hexafluoride (n-Bu_4NPF_6, 0.1 M) in acetonitrile was employed as the supporting electrolyte, and the scan rate was kept at 100 mV s^{-1}. Electrochemically reversible ferrocene was employed as internal reference. The HOMO and LUMO energy levels were calculated from the onset oxidation and the onset reduction potentials, respectively, by following the equation $E_{HOMO} = -(4.80+E_{ox}^{onset})$ eV, $E_{LUMO} = -(4.80+E_{re}^{onset})$ eV.

Atomic force microscopy (AFM). The AFM images were performed using in tapping mode on a Bruker Dimension Icon atomic force microscope.

Grazing incidence wide angle X-ray scattering (GIWAXS). The GIWAXS samples were deposited on Si substrates by the same preparation conditions with devices. The GIWAXS data were obtained at 1W1A Diffuse X-ray Scattering Station, Beijing Synchrotron Radiation Facility (BSRF-1W1A).

Photoluminescence (PL). The PL measurements were conducted by using FLS1000 equipment. The emission spectra of CH8-0, CH8-1 and CH8-2 were obtained using the same setup used for recording electroluminescence spectra excited by a 765 nm wavelength provided by Xenon lamp. (Detector for NIR 5509 PMT, 600-1700 nm).

Electroluminescence (EL). The OSCs used for the EL spectra measurements are the same with those of the *J-V* measurements, with the conversional device structure of ITO/PEDOT:PSS (4083)/PM6:NFAs / PNDIT-F3N/Ag. The EL spectra are measured by using a source meter (Keithley 2400) to inject electric current (1 mA), and the emitted photons were measured using a fluorescence spectrometer (KYMERA- 328I-B2, Andor technology LTD) with two sets of diffraction gratings, coupled to a Si EMCCD camera (DU970P-BVF, Andor) for the wavelength range of 400-1000 nm,

and an InGaAs camera (DU491A-1.7, Andor) for the wavelength range of 900-1700 nm was used to collect the photons emitted from the solar cell.

EQE_{EL}. For the EQE_{EL} measurements, a digital source meter (Keithley 2400) was employed to inject electric current into the solar cells, and the emitted photons were collected by a Si diode (Hamamatsu s1337-1010BQ) and indicated by a picoammeter (Keithley 6482).

Highly sensitive EQE (sEQE). sEQE measurements were conducted by using a measurement system containing a halogen lamp light source (LSH-75, Newport), a monochromator (CS260-RG-3-MC-A, Newport), a current amplifier, a chopper and a phase-locked amplifier (SR830, Newport). The overtone signals from the monochromator were blocked by a group of long pass filters (1100 nm, 900 nm, 600 nm).

Device fabrication and measurement. The conventional devices were fabricated with an architecture of ITO/PEDOT:PSS (4083)/PM6: Acceptors/PNDIT-F3N/Ag. In detail, the ITO glass was pre-cleaned in turn in an ultrasonic bath of detergent, deionized water, acetone and isopropanol. Then the surface of ITO was treated by UV light in an ultraviolet-ozone chamber (Jelight Company) for 15 min. A thin layer of poly(3,4-ethylene dioxythiophene):poly(styrene sulfonate) (PEDOT:PSS, Baytron PVP Al 4083) was prepared by spin-coating the PEDOT:PSS solution at 4300 rpm for 20 s on the ITO substrate. Note that the PEDOT:PSS solution was pre-filtered through a 0.45 um poly(tetrafluoroethylene) (PTFE) filter. Subsequently, the PEDOT:PSS films were baked at 150 ℃ for 20 min in air and transferred to a glove box filled with nitrogen. The PM6:CH8-0 (D/A 1:1) with 0.3% 1-chloronaphthalene, PM6:CH8-1 (D/A 1:1) with 0.3% 1-chloronaphthalene and PM6:CH8-0 (D/A 1:1.2) with 0.5% 1-chloronaphthalene mixtures were fully dissolved in chloroform (CF) at a concentration of 6 mg/mL of PM6 respectively, and the resulting solutions were spin-casted at 2000 rpm for 30 s onto the PEDOT:PSS layer. Then the films were treated with the thermal annealing at 90˚C for 10 min. The thickness of all active layers was controlled to be ~100 nm. After that, a thin layer of PNDIT-F3N (dissolved in

methanol with the concentration of 1 mg/mL) was spin-coated on the top of the active layer. Finally, a layer of Ag with thickness of 150 nm was deposited under 2×10^{-6} Pa. The active area of the device was 2.56 mm^2. The current density-voltage (*J-V*) curves of photovoltaic devices were recorded by a Keithley 2400 source-measure unit. The photocurrent was measured under the simulated illumination of 100 mW cm^{-2} with AM1.5 G using a Enli SS-F5-3A solar simulator, which was calibrated by a standard Si solar cell (made by Enli Technology Co., Ltd., Taiwan, and calibrated report can be traced to NREL). The thickness of the active layers was measured by a Veeco Dektak 150 profilometer. The EQE spectra were measured by using a QE-R Solar Cell. Response Measurement System (Enli Technology Co., Ltd., Taiwan).

Space-charge-limited current (SCLC) measurement. The SCLC method was used to measure the hole and electron mobilities, by using a diode configuration of ITO /PEDOT:PSS/active layer/MoO_3/Al for hole-only device and ITO/ZnO/active layer/ PNDIT-F3N/Al for electron-only device. In our case, we applied forward scans for all the SCLC measurements, and hence the ITO and Al electrodes should be the anode and cathode, respectively. The dark current density curves were recorded with a bias voltage in the range of 0-8 V. The mobilities were estimated by taking current-voltage curves and fitting the results based on the equation listed below:

$$J = \frac{9\varepsilon_0\varepsilon_\gamma\mu V^2}{8L^3}$$

where J is the current density, ε_0 is the vacuum permittivity, ε_r is the relative dielectric constant, μ is the mobility, and L is the film thickness. V ($=V_{app}-V_{bi}$) is the internal voltage in the device, where V_{app} is the applied voltage to the device and V_{bi} is the built-in voltage due to the relative work function difference of the two electrodes.

2. Synthesis of CH8-0, CH8-1 and CH8-2.

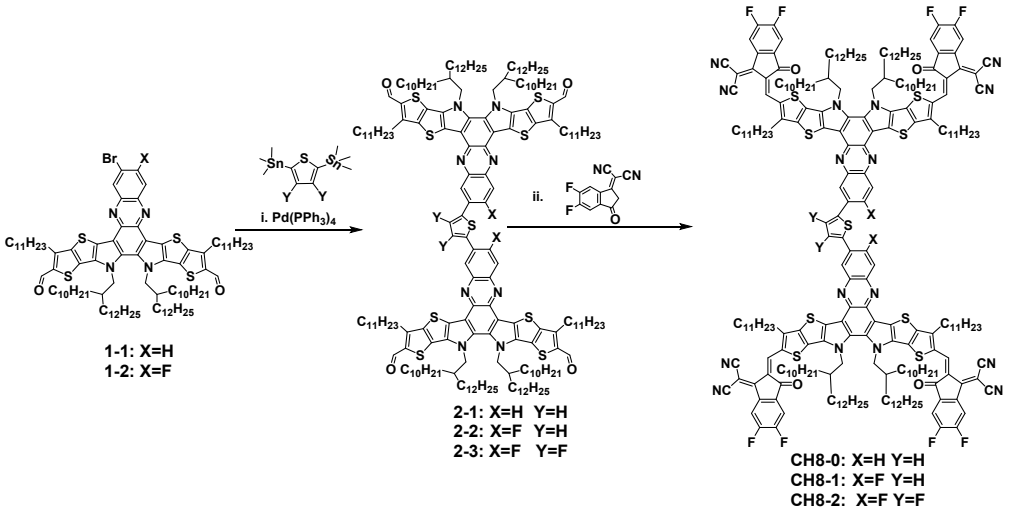

Scheme S1. The overall synthetic route to CH8-0, CH8-1 and CH8-2. Reagents and conditions: (i) $Pd(PPh_3)_4$, 2,5-bis(trimethylstannyl)thiophene or 3,4-difluoro-2,5-bis(trimethylstannyl)thiophene, toluene, reflux; (ii) 2-(5,6-difluoro-3-oxo-2,3-dihydro-1H-inden-1-ylidene)malononitrile, pyridine, $CHCl_3$, reflux.

Synthesis of compound 2-1, 2-2 and 2-3. Compound 1-1 (400 mg, 0.25 mmol, 1.0 eq.), 2,5-bis(trimethylstannyl)thiophene (51 mg, 0.125 mmol, 0.5 eq.), $Pd(PPh_3)_4$ (58 mg, 0.05 mmol, 0.2 eq.) and 30 mL dry toluene were added to 100 mL two-necked round bottom flask and the resulting mixture was purged with argon for 10 mins. Then the mixture was heated to reflux for 12 h. After cooling to room temperature, the reaction mixture was precipitated in 50 mL methanol. The precipitate was purified by column chromatography on silica gel with petroleum ether/dichloromethane (*v*/*v*=3/2) as eluent to give red compound 2-1 (262 mg, 67%). Compound 2-2 was obtained by a similar method with a yield of 64% as a red solid. Compound 2-3 was obtained by a similar method with a yield of 59% as a red solid.

Data for compound 2-1: ^{1}H NMR (400 MHz, $CDCl_3$) δ 10.16 (s, 4H), 8.68 (s, 2H), 8.46 (d, *J* = 8.1 Hz, 2H), 8.23 (d, *J* = 8.7 Hz, 2H), 7.73 (s, 2H), 4.72 (s, 8H), 3.26 (d, *J* = 6.0 Hz, 8H), 2.17 (s, 4H), 2.00 (d, *J* = 6.2 Hz, 8H), 1.54-1.43 (m, 18H), 1.29-0.83 (m, 242H). ^{13}C NMR (101 MHz, $CDCl_3$) δ 181.63, 146.87, 146.81, 144.21, 144.14, 141.91, 141.40, 138.81, 137.91, 136.78, 136.72, 134.34, 132.86, 132.66, 130.00, 129.56, 128.21, 128.07, 127.19, 125.94, 124.31, 118.17, 117.96,

55.39, 38.98, 31.93, 31.91, 31.87, 30.62, 30.56, 30.48, 29.69, 29.63, 29.57, 29.49, 29.43, 29.35, 29.26, 28.22, 25.59, 22.69, 22.66, 14.11. MS (*m*/*z*, MALDI): Calc. for $[C_{196}H_{300}N_8O_4S_9]H^+$ 3121.11, found: 3121.68.

Data for compound 2-2: ^{1}H NMR (400 MHz, $CDCl_3$) δ 10.16 (s, 4H), 8.81 (d, *J* = 6.9 Hz, 2H), 8.20 (d, *J* = 12.0 Hz, 2H), 7.94 (s, 2H), 4.70 (d, *J* = 5.3 Hz, 8H), 3.26 (s, 8H), 2.15 (s, 4H), 1.99 (s, 8H), 1.62-1.42 (m, 26H), 1.29-0.84 (m, 234H). ^{13}C NMR (101 MHz, $CDCl_3$) δ 181.69, 158.12, 146.91, 146.86, 144.24, 144.22, 139.00, 138.50, 138.48, 138.46, 138.36, 136.85, 136.81, 136.78, 133.04, 132.68, 129.55, 128.15, 128.08, 117.91, 117.74, 55.40, 38.94, 31.94, 31.90, 31.87, 30.60, 30.45, 29.75, 29.69, 29.66, 29.64, 29.59, 29.53, 29.50, 29.44, 29.38, 29.35, 29.31, 29.28, 28.23, 25.56, 22.70, 22.68, 22.65, 14.12. MS (*m*/*z*, MALDI): Calc. for $[C_{196}H_{298}F_2N_8O_4S_9]H^+$ 3157.10, found: 3157.52.

Data for compound 2-3: ^{1}H NMR (400 MHz, $CDCl_3$) δ 10.14 (s, 4H), 8.85 (s, 2H), 8.17 (d, *J* = 9.0 Hz, 2H), 4.70 (d, *J* = 5.9 Hz, 8H), 3.24 (s, 8H), 2.15 (s, 4H), 1.97 (s, 8H), 1.64 (s, 2H), 1.52-1.41 (m, 18H), 1.31-0.82 (m, 240H). ^{13}C NMR (101 MHz, $CDCl_3$) δ 181.65, 160.04, 157.50, 146.88, 146.83, 144.33, 144.24, 142.26, 142.06, 141.66, 141.53, 138.86, 138.64, 138.53, 136.86, 136.75, 133.21, 132.65, 130.06, 129.46, 128.18, 128.09, 121.75, 121.57, 117.86, 117.57, 114.67, 113.30, 113.08, 55.44, 38.98, 31.92, 31.88, 30.62, 30.55, 30.47, 29.74, 29.68, 29.63, 29.57, 29.52, 29.49, 29.45, 29.35, 29.31, 29.26, 28.21, 25.58, 22.68, 22.65, 14.09. MS (*m*/*z*, MALDI): Calc. for $[C_{196}H_{296}F_4N_8O_4S_9]H^+$ 3193.08, found: 3193.52.

Synthesis of compound CH8-0, CH8-1 and CH8-2. Under argon protection, compound 2-1 (221 mg, 0.07 mmol, 1.0 eq.), 2-(5,6-difluoro-3-oxo-2,3-dihydro-1H-inden-1-ylidene)malononitrile (196 mg, 0.85 mmol, 12 eq.) and 30 mL dry chloroform were added to 100 mL two-necked round bottom flask. Then 0.5 mL pyridine was dropped into the mixture. The reaction mixture was stirred at 70 ℃ for 12 h. After cooling to room temperature, the reaction mixture was precipitated in 70 mL methanol. The precipitate was purified by column chromatography on silica gel with petroleum ether/ chloroform (v/v=4/5) as eluent to give black compound CH8-0 (182 mg, 79%); Compound CH8-1 was obtained by a similar method with a yield of

76% as a black solid. Compound CH8-2 was obtained by a similar method with a yield of 82% as a black solid.

Data for compound CH8-0: MS (*m*/*z*, MALDI): Calc. for $C_{244}H_{308}F_8N_{16}O_4S_9$ 3966.17, found: 3966.21. Data for compound CH8-1 MS (*m*/*z*, MALDI): Calc. for $C_{244}H_{306}F_{10}N_{16}O_4S_9$ 4002.16, found: 4002.76. Data for compound CH8-2: MS (*m*/*z*, MALDI): Calc. for $C_{244}H_{304}F_{12}N_{16}O_4S_9$ 4038.14, found: 4038.22.

3. Figures and Tables.

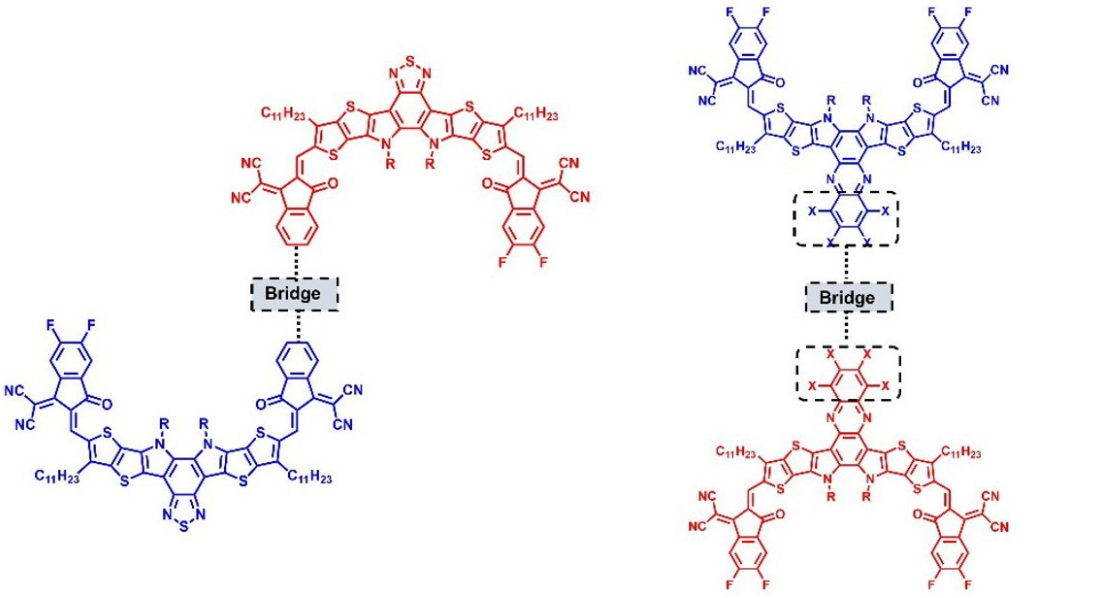

Figure S1. A comparison of connection modes in this and other works. The red and blue represent two monomers, respectively.

3.1 Photophysical properties of CH8-0, CH8-1 and CH8-2.

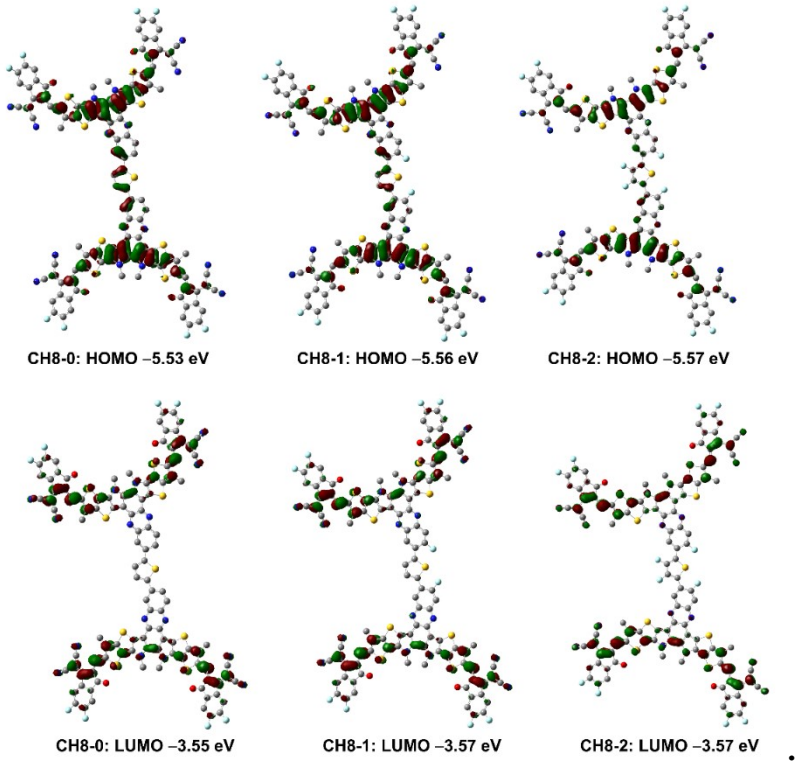

Figure S2. Theoretical density distribution for the frontier molecular orbits of CH8-0, CH8-1 and CH8-2.

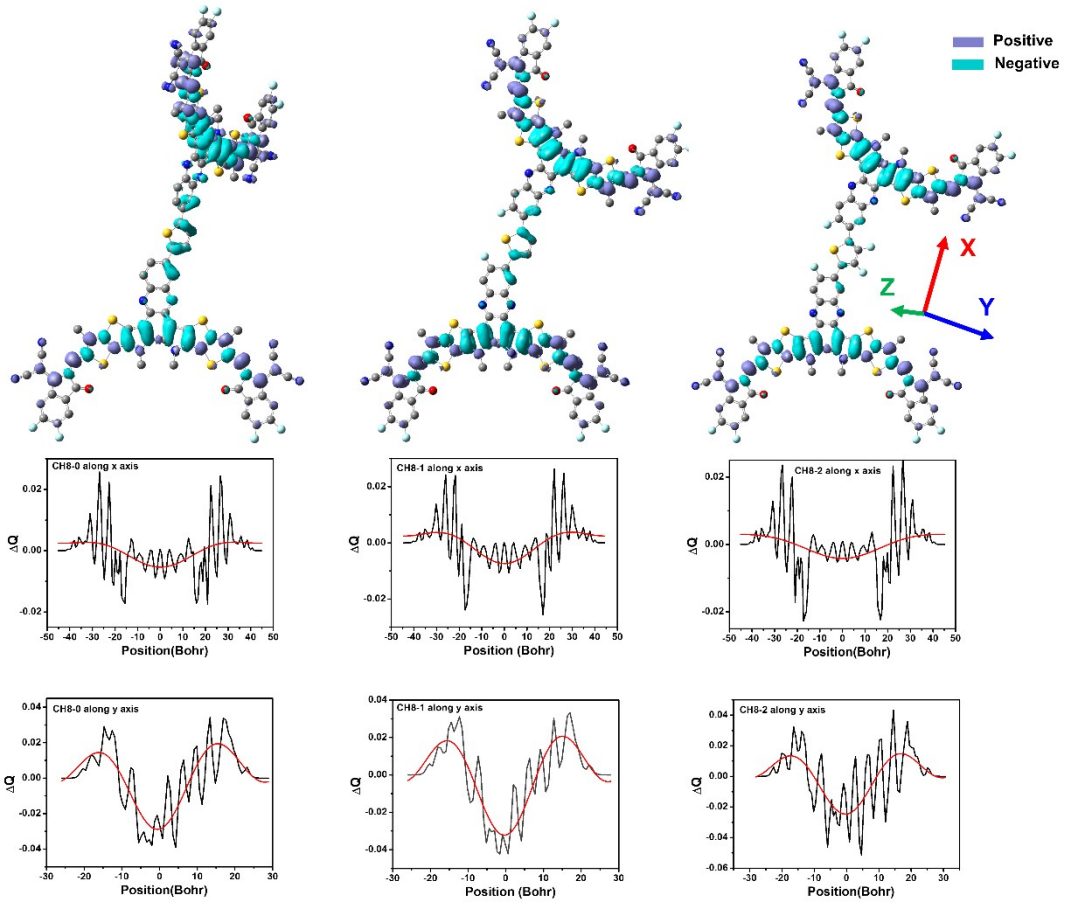

Figure S3. Theoretical density distribution ΔQ (ΔQ = Ψ^2_{LUMO}—Ψ^2_{HOMO}) along x and y axis of CH8-0, CH8-1 and CH8-2. Charge density difference ΔQ (ΔQ = Ψ^2_{LUMO}— Ψ^2_{HOMO}) x and y axis (backbone) of the defined molecules. Black curves are the integral lines of the charge density difference (ΔQ) along x or y axis (backbone) of the defined molecules. Red curves are the simulated results with low frequencies wave functions by fast fourier transform filters.[5]

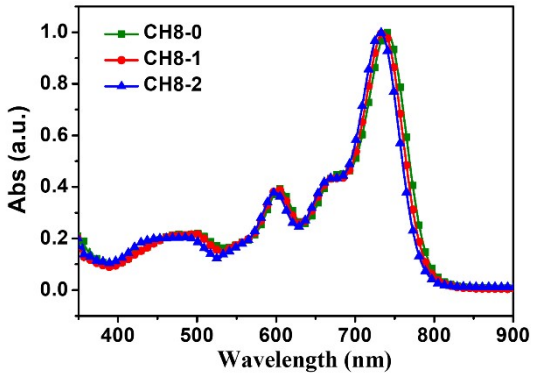

Figure S4. Normalized absorption spectra of CH8-0, CH8-1 and CH8-2 in dilute chloroform solution.

Table S1. The optical and electrochemical data of acceptors in this work.

Comp	$\lambda_{max}^{sol[a]}$ (nm)	$\lambda_{max}^{film[b]}$ (nm)	λ_{edg}^{film} (nm)	$E_g^{onset[c]}$ (eV)	HOMO[d] (eV)	LUMO[d] (eV)	$\varepsilon^{[e]}$ (10^5 M^{-1} cm^{-1})
CH8-0	740	801	881	1.41	–5.61	–3.78	3.78
CH8-1	736	788	871	1.42	–5.69	–3.80	3.93
CH8-2	732	788	863	1.44	–5.71	–3.81	3.96

[a] λ_{max}^{sol} was obtained from UV-*Vis* absorption spectra of CH8-0, CH8-1 and CH8-2 in chloroform solutions. [b] λ_{max}^{film} was obtained from UV-*Vis* absorption spectra of CH8-0, CH8-1 and CH8-2 in films. [c] Optical band gap (E_g^{onset}) was calculated by $1240/\lambda_{edge}^{film}$. [d] The highest occupied molecular orbital (HOMO) and lowest unoccupied molecular orbital (LUMO) energy levels were calculated from the onset oxidation potential and the onset reduction potential using the equation E_{HOMO} = - (4.80+E_{ox}^{onset}) eV, E_{LUMO} = - (4.80+E_{re}^{onset}) eV. [e] ε is molar extinction coefficient obtained from UV-Vis absorption spectra of CH8-0, CH8-1 and CH8-2 in chloroform solution.

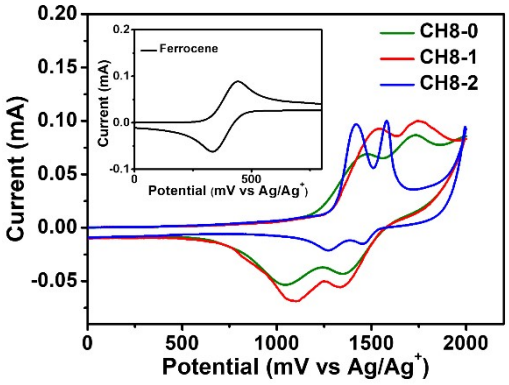

Figure S5. Cyclic voltammograms of the reference (ferrocene) and CH8-0, CH8-1 and CH8-2 films. Ferrocene: oxidation and reduction cycle; CH8-0, CH8-1 and CH8-2 films: oxidation cycle. All measurements were conducted at room temperature with a three-electrode configuration, including a glassy carbon electrode as the working electrode, a saturated calomel electrode (SCE) as the reference electrode, and a Pt wire as the counter electrode. Tetrabutyl ammonium phosphorus hexafluoride (*n*-Bu_4NPF_6, 0.1 M) in acetonitrile was employed as the supporting electrolyte, and the scan rate was kept at 100 mV s^{-1}. Electrochemically reversible ferrocene was employed as internal reference. The HOMO and LUMO energy levels were calculated from the onset oxidation and the onset reduction potentials, respectively, by following the equation $E_{HOMO} = -(4.80+E_{ox}^{onset})$ eV, $E_{LUMO} = -(4.80+E_{re}^{onset})$ eV.

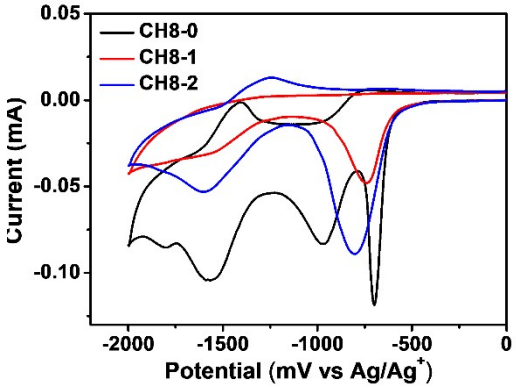

Figure S6. Cyclic voltammograms of CH8-0, CH8-1 and CH8-2 films (reduction cycle). The details on the CV measurements are the same to those in Figure S5.

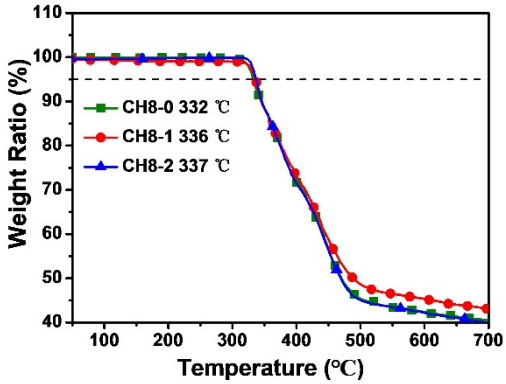

Figure S7. Thermogravimetric analysis (TGA) curves of CH8-0, CH8-1 and CH8-2. The heating rate is a heating rate of 10 ºC/min under nitrogen atmosphere.

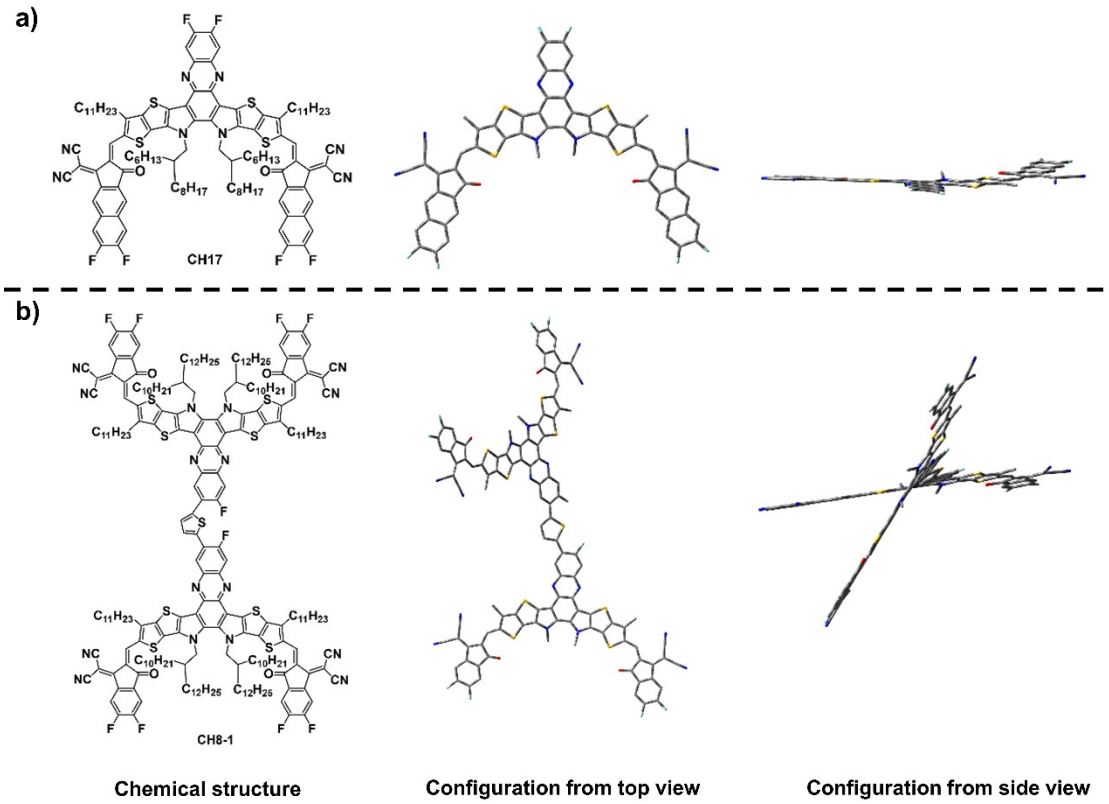

Figure S8. Molecular structures and configurations of CH17 and CH8-1. (a) CH17; (b) CH8-1.

3.2 Photovoltaic device performance.

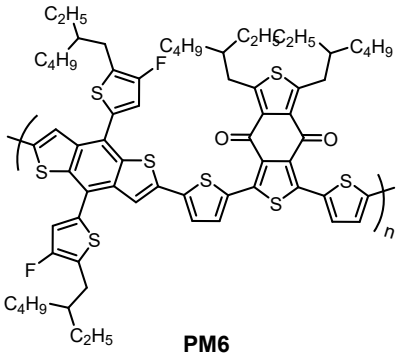

Figure S9. Chemical structure of polymer donor PM6.

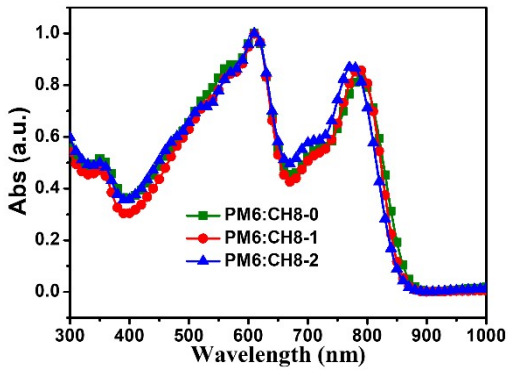

Figure S10. Normalized absorption spectra of blended films.

Table S2. Detailed photovoltaic parameters of the PM6:CH8-0 based devices by optimal conditions under illumination of AM 1.5 G, 100 mW/cm^2. [a]

Active layer	V_{oc} [V]	FF [%]	J_{sc} [mA cm^{-2}]	PCE [%]
PM6:CH8-0	0.935	72.0	22.42	15.09
	0.933	70.9	22.39	14.82
	0.933	71.1	22.88	15.19
	0.932	70.6	23.07	15.18
	0.932	70.9	22.83	15.09
	0.936	72.1	22.61	15.26
	0.934	71.8	22.50	15.10
	0.932	71.3	22.46	14.92
	0.933	71.5	22.26	14.85
	0.931	72.5	22.47	15.15
	0.932	71.7	22.62	15.10
	0.930	71.5	22.60	15.03
	0.931	71.8	22.40	14.96
	0.934	70.4	22.69	14.91
	0.930	71.0	22.93	15.15
Average[b]	0.932	71.4	22.61	15.05

[a]The device architecture is ITO/PEDOT:PSS/active layer (D:A=1:1)/PNDIT-F3N/Ag; D = 6 mg/mL in chloroform with 0.3 vol% CN; the resulting solutions were spin-casted at 2000 rpm onto the PEDOT:PSS layer; TA (90 ℃ for 10 min). [b] The average values are obtained from 15 devices.

Table S3. Detailed photovoltaic parameters of the PM6:CH8-1 based devices by optimal conditions under illumination of AM 1.5 G, 100 mW/cm^2. [a]

Active layer	V_{oc} [V]	FF [%]	J_{sc} [mA cm^{-2}]	PCE [%]
PM6:CH8-1	0.930	75.6	23.63	16.63
	0.928	75.5	23.78	16.67
	0.933	75.8	23.64	16.74
	0.926	73.6	24.81	16.91
	0.924	73.8	24.76	16.89
	0.922	73.6	24.96	16.94
	0.927	73.2	24.71	16.77
	0.923	74.2	24.89	17.05
	0.921	74.4	24.82	17.00
	0.918	74.3	24.91	16.98
	0.917	74.1	24.92	16.94
	0.929	74.2	24.34	16.77
	0.931	73.6	24.71	16.93
	0.931	74	24.61	16.97
	0.929	73.7	24.62	16.88
Average[b]	0.926	74.2	24.54	16.87

[a]The device architecture is ITO/PEDOT:PSS/active layer (D:A=1:1)/PNDIT-F3N/Ag; D=6 mg/mL in chloroform with 0.5 vol% CN; the resulting solutions were spin-casted at 2000 rpm onto the PEDOT:PSS layer; TA (90 ℃ for 10 min). [b] The average values are obtained from 15 devices.

Table S4. Detailed photovoltaic parameters of the PM6:CH8-2 based devices by optimal conditions under illumination of AM 1.5 G, 100 mW/cm^2. [a]

Active layer	V_{oc} [V]	FF [%]	J_{sc} [mA cm^{-2}]	PCE [%]
PM6:CH8-2	0.927	75.2	23.95	16.70
	0.924	74.8	23.89	16.52
	0.923	74.5	24.39	16.77
	0.921	74.2	24.53	16.76
	0.920	74.2	24.39	16.66
	0.928	74.8	23.98	16.64
	0.927	74.7	24.35	16.84
	0.927	74.8	23.83	16.53
	0.925	74.8	24.13	16.70
	0.923	74.3	24.29	16.67
	0.921	74.2	24.27	16.59
	0.921	74.4	24.06	16.48
	0.934	72.1	24.84	16.71
	0.929	72.1	24.52	16.42
	0.927	71.9	24.63	16.41
Average[b]	0.925	74.1	24.27	16.63

[a]The device architecture is ITO/PEDOT:PSS/active layer (D:A=1:1.2)/PNDIT-F3N/Ag; D=6 mg/mL in chloroform with 0.3 vol% CN; the resulting solutions were spin-casted at 2000 rpm onto the PEDOT:PSS layer; TA (90 ℃ for 10 min). [b] The average values are obtained from 15 devices.

Table S5. Detailed photovoltaic parameters of the PM6:CH8-0 based devices processed by varied conditions under illumination of AM 1.5 G, 100 mW/cm^2.

D/A [*w*/*w*]	CN [*v*/*v*]	TA[°C]	V_{oc} [V]	J_{sc} [mA cm^{-2}]	FF [%]	PCE [%]
1:0.8	-	-	0.927	20.89	67.7	13.12
1:1	-	-	0.921	21.40	67.7	13.34
1:1.2			0.920	21.31	66.4	13.02
1:1.4	-	-	0.921	20.81	67.0	12.83
1:1	0.3%	80	0.938	22.57	70.5	14.88
	0.5%	80	0.938	21.67	71.1	14.46
	0.7%	80	0.937	21.52	70.5	14.22
	0.3%	90	0.936	22.61	72.1	15.26
	0.3%	100	0.928	22.81	71.5	15.15

Table S6. Detailed photovoltaic parameters of the PM6:CH8-1 based devices processed by varied conditions under illumination of AM 1.5 G, 100 mW/cm^2.

D/A [*w*/*w*]	CN [*v*/*v*]	TA[°C]	V_{oc} [V]	J_{sc} [mA cm^{-2}]	FF [%]	PCE [%]
1:0.8	-	-	0.947	21.87	69.7	14.45
1:1	-	-	0.946	23.08	69.3	15.14
1:1.2	-	-	0.943	22.88	65.3	14.08
1:1	0.3%	90	0.922	23.67	72.6	15.84
	0.5%	90	0.923	24.89	74.2	17.05
	0.7%	90	0.924	24.25	74.4	16.67
	0.3%	80	0.922	23.62	74.7	16.39
	0.3%	100	0.921	23.31	75.2	16.14

Table S7. Detailed photovoltaic parameters of the PM6:CH8-2 based devices processed by varied conditions under illumination of AM 1.5 G, 100 mW/cm^2.

D/A [*w*/*w*]	CN [*v*/*v*]	TA[°C]	V_{oc} [V]	J_{sc} [mA cm^{-2}]	FF [%]	PCE [%]
1:0.8	-	-	0.953	21.23	69.5	14.06
1:1	-	-	0.950	21.84	68.9	14.29
1:1.2			0.947	22.61	68.3	14.62
1:1.4	-	-	0.946	22.12	67.4	14.10
1:1.2	0.2%	90	0.930	24.62	71.4	16.36
	0.3%	90	0.928	24.24	74.9	16.84
	0.5%	90	0.928	24.57	71.5	16.30
	0.3%	80	0.932	23.96	72.8	16.26
	0.3%	100	0.917	24.57	71.5	16.30
	0.3%	110	0.910	24.55	70.0	15.65

Table S8. A summary of the J_{SC} and PCE of binary BHJ OSCs based on multi-dimensional acceptors.

Active layer	V_{OC} [V]	J_{SC} [mA cm^{-2}]	FF [%]	PCE [%]	Ref
PBDB-T:TITTOT-ICF	0.83	16.95	59	8.23	1[6]
PTTEA:TTC-3PDI	1.06	12.19	67.78	8.75	2[7]
PTTEA:TTC-3PDI-3N	1.12	13.09	71.76	10.52	2[7]
PM6/FBTIC	0.908	14.6	66.6	8.84	3[8]
PTB7-Th:TPDI2	0.777	15.85	62.55	7.84	4[9]
PTB7-Th:FTPDI2	0.790	16.77	61.67	8.28	4[9]
J61:BTCDT-ICF	0.73	16.93	65.6	8.11	5[10]
PTB7-Th:TPDI2-Se	0.794	17.21	60.3	8.59	6[11]
PM6:FBTIC	0.947	14.1	75.4	10.1	7[12]
PTB7-Th:Para-TrBRCN	0.95	13.75	63.5	8.29	8[13]
PTB7-Th:Meta-TrBRCN	0.94	16.75	64.5	10.15	8[13]
DBFI-EDOT:PSEHTT	0.93	13.82	63	8.10	9[14]
PTB7-Th:Ta-PDI	0.78	17.10	68.5	8.91	10[15]
P3HT:TrBTIC	0.88	13.04	71.9	8.25	11[16]
D18-Cl-B:4A-DFIC	0.905	22.47	77.4	15.76	12[17]
PTB7-Th:TPDI3	0.783	16.75	67.4	8.84	14[18]
P3TEA:CRP-1	1.06	15.32	68.4	11.2	15[19]
P3TEA:CRP-2	1.06	14.98	64.6	10.3	15[19]
PBDB-T:B3T-TT-6F	0.819	18.28	66.41	9.94	16[20]
PBDB-T:B3T-BT-6F	0.807	16.53	63.48	8.40	16[20]
PDBT-T1:TPH-Se 6a	1.00	12.53	71.7	9.28	18[21]
P3TEA:FTTB-PDI4	1.13	13.89	65.9	10.58	19[22]
PBDB-T:NTPH-P	1.00	13.32	61	8.11	21[23]
PM6:CH8	0.889	19.7	53.5	9.37	23[24]
PM6:CH8-0	0.936	22.61	72.1	15.26	This work
PM6:CH8-1	0.923	24.98	74.2	17.05	This work
PM6:CH8-2	0.928	24.24	74.9	16.84	This work

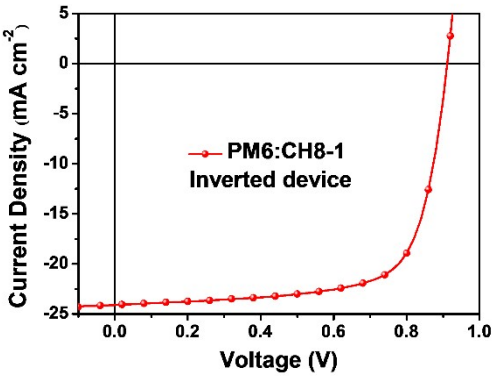

Figure S11. The *J-V* curve of OSCs based on PM6:CH8-1 by using an inverted device structure of ITO/ZnO/PFN-Br/ Active layer /MoOx/Ag .

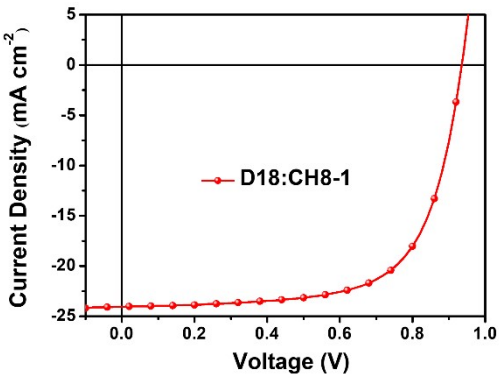

Figure S12. The *J-V* curve of OSCs based on D18:CH8-1 by using a conventional architecture of ITO Glass/PEDOT:PSS/Active layer/PNDIT-F3N/Ag.

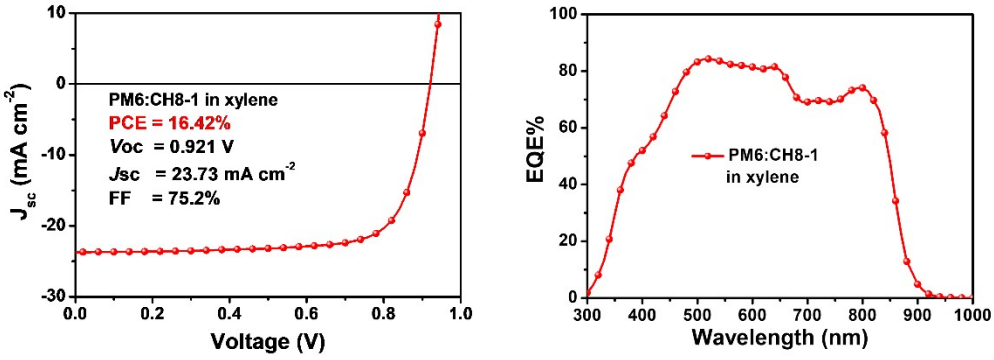

Figure S13. The *J-V* and EQE curves of PM6:CH8-1 device in o-xylene using a conventional architecture of ITO Glass/PEDOT:PSS/Active layer/PNDIT-F3N/Ag. The PM6:CH8-1 (D/A 1:1) with 50% 2-Methoxynaphthalene mixtures were fully dissolved in o-xylene at a concentration of 7 mg/mL of PM6, and the resulting solutions was heated 2h under a temperature of 60 ℃. Then the system were cooled to 35 ℃ and spin-casted at 2100 rpm for 30 s onto the PEDOT:PSS layer. Then the films were treated with the thermal annealing at 90˚C for 10 min. After that, a thin layer of PNDIT-F3N (dissolved in methanol with the concentration of 1 mg/mL) was spin-coated on the top of the active layer.

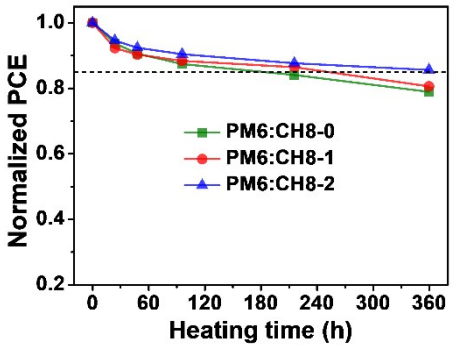

Figure S14. The PCE variation versus the operating time for OSCs measured in a glovebox filled with nitrogen at 65℃.

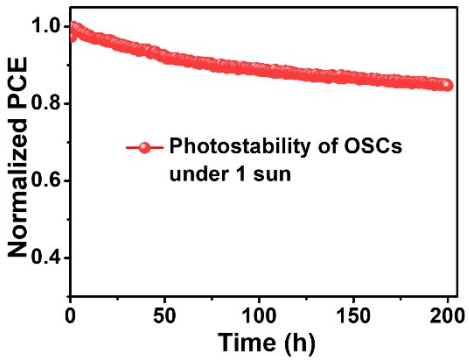

Figure S15. The PCE variation of OSCs based on PM6:CH8-1 versus the operating time in a glovebox filled with nitrogen under 1 sun illumination.

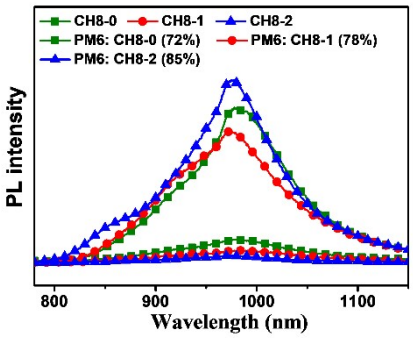

Figure S16. Photoluminescence spectra of neat and blend films.

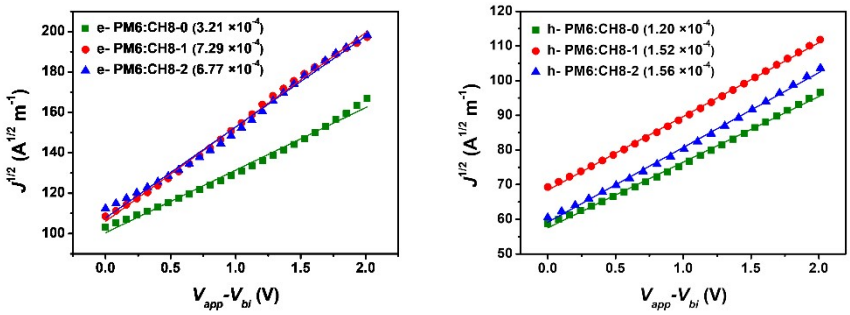

Figure S17. SCLC characteristics of electron-only and hole-only of PM6:CH8-0, PM6:CH8-1 and PM6:CH8-2 blend films. The μ_e/μ_h ratios of PM6:CH8-0, PM6:CH8-1 and PM6:CH8-2 blends are 2.7, 4.8 and 4.3, respectively.

Table S9. Charge carrier transport parameters of the optimized BHJ blends and devices.

Blend Films	μ_e[a] (10^{-4} cm^2 V^{-1} s^{-1})	μ_h[a] (10^{-4} cm^2 V^{-1} s^{-1})	μ_e/μ_h	η_{diss}[b] (%)	η_{coll}[b] (%)	α[c] (%)	η_{PLQ}[d] (%)
PM6:CH8-0	3.21	1.20	2.7	95.3	83.2	98.9	72
PM6:CH8-1	7.29	1.52	4.8	97.0	84.9	99.3	78
PM6:CH8-2	6.77	1.56	4.3	97.2	87.2	99.3	85

[a] μ_e and μ_h are electron and hole mobilities of optimized PM6:CH8-0, PM6:CH8-1 and PM6:CH8-2 blends by SCLC measurements. [b] η_{diss} and η_{coll} are J_{ph}/J_{sat} obtained from J_{ph}-V_{eff} pots of optimized OSCs under maximal power output condition and the short-circuit condition. [c] α was obtained from pots of dependence of current density (J_{sc}) on P_{light} of optimized OSCs. [d] η_{PLQ} is fluorescence quenching efficiency of corresponding blend films.

Table S10. Electron reorganization energies (λ) of some representative acceptors.[1, 24-27]

Acceptors	λ meV
$PC_{61}BM$	154
ITIC	155
ITIC-4F	158
Y6	150
BT-L4F	132
BT-BO-L4F	133
CH-4Cl	135
CH-6Cl	136
CH17	126
CH8-0	74
CH8-1	75
CH8-2	76

Table S11. Total energy loss values and different contributions in solar cells based on the SQ limit theory.

Active layer	V_{OC} (V)	E_g[a] (eV)	$V_{OC,}$ SQ[b] (V)	$V_{OC,}$ rad[b] (V)	ΔE_1[c] (eV)	ΔE_2[d] (eV)	ΔE_3[e] (eV)	E_{loss}[f] (eV)
PM6:CH8-0	0.936	1.426	1.162	1.118	0.264	0.044	0.182	0.490
PM6:CH8-1	0.923	1.441	1.176	1.129	0.265	0.047	0.206	0.518
PM6:CH8-2	0.928	1.458	1.191	1.141	0.266	0.050	0.213	0.530

[a] E_g is estimated on the basis of the derivatives of the EQE spectra (dEQE/dE, black curves) (Figure S11).[28] [b] V_{OC}^{SQ} is the upper limit for the V_{OC} of the solar cell derived in the Shockley-Quessier theory. V_{OC}^{rad} is the radiative recombination limit for the V_{OC} of the solar cell, which can be determined by the equation:

$$V_{OC}^{SQ} = \frac{kT}{q}\ln\left(\frac{J_{SC}^{SQ}}{J_0^{SQ}} + 1\right) \cong \frac{kT}{q}\ln\left(\frac{q\cdot\int_{E_g}^{+\infty}\emptyset_{AM1.5G}(E)dE}{q\cdot\int_{E_g}^{+\infty}\emptyset_{BB}(E)dE}\right)$$ [c]

$\Delta E_1 = E_g - qV_{OC}^{SQ}$; [d] $\Delta E_2 = qV_{OC}^{SQ} - qV_{OC}^{rad}$; $J_{0,\mathrm{rad}} = q\int \mathrm{EQE}(E)\emptyset_{\mathrm{BB}}(E)\mathrm{d}E$; $V_{\mathrm{OC}}^{\mathrm{rad}} = \frac{k_{\mathrm{B}}T}{q}\mathrm{In}(\frac{J_{\mathrm{SC}}}{J_{0,\mathrm{rad}}} + 1)$ [e]

$\Delta E_3 = qV_{\mathrm{OC}}^{\mathrm{rad}} - qV_{\mathrm{OC}}$[f] $E_{\mathrm{loss}} = \Delta E_1 + \Delta E_2 + \Delta E_3$.[29]

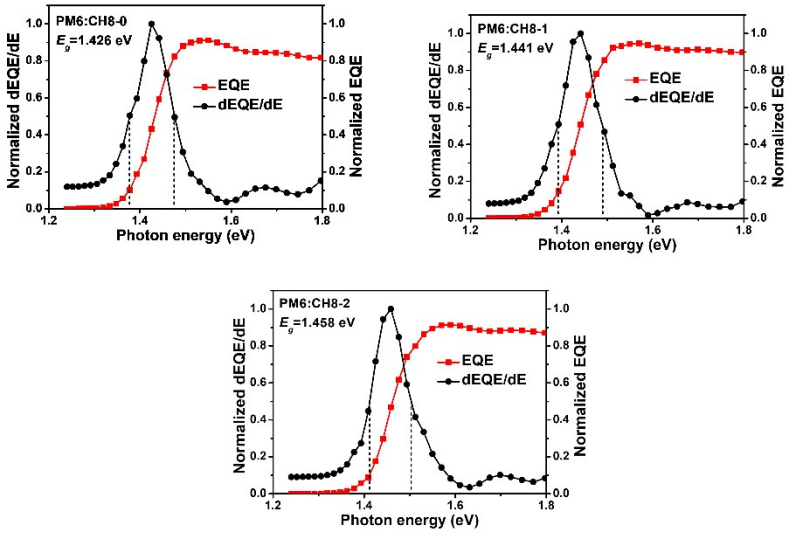

Figure S18. Optical bandgap determination of PM6:CH8-0, PM6:CH8-1and PM6:CH8-2 on the basis of the derivatives of the EQE spectra (dEQE/dE, black curves). The region between dashed lines is the part where the gap distribution probability is greater than half of the maximum, which is used for the bandgap calculation.[28]

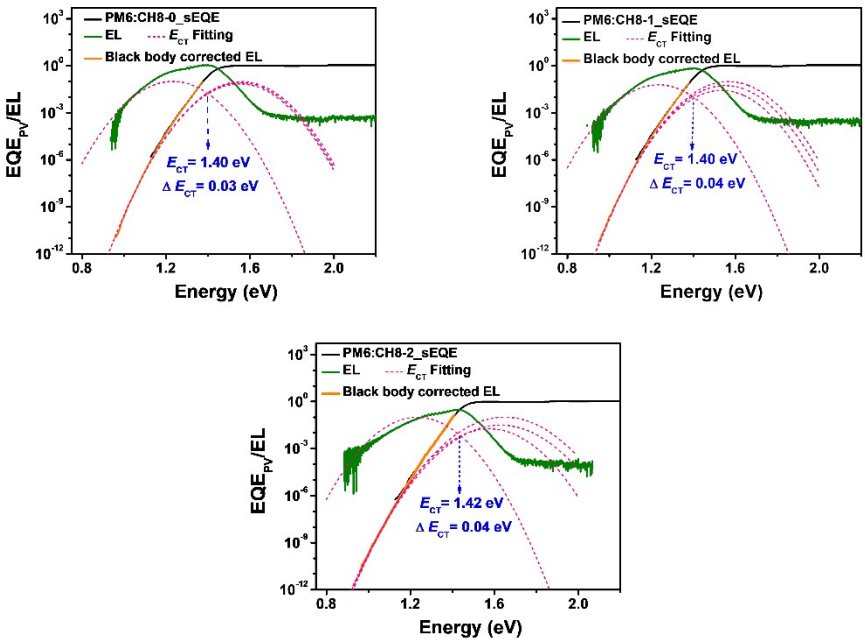

Figure S19. Sensitive external quantum efficiency (sEQE) spectra and the fitting results for the relevant devices. ΔE_{CT}= E_g-E_{CT} (E_g is afforded in Figure S11).

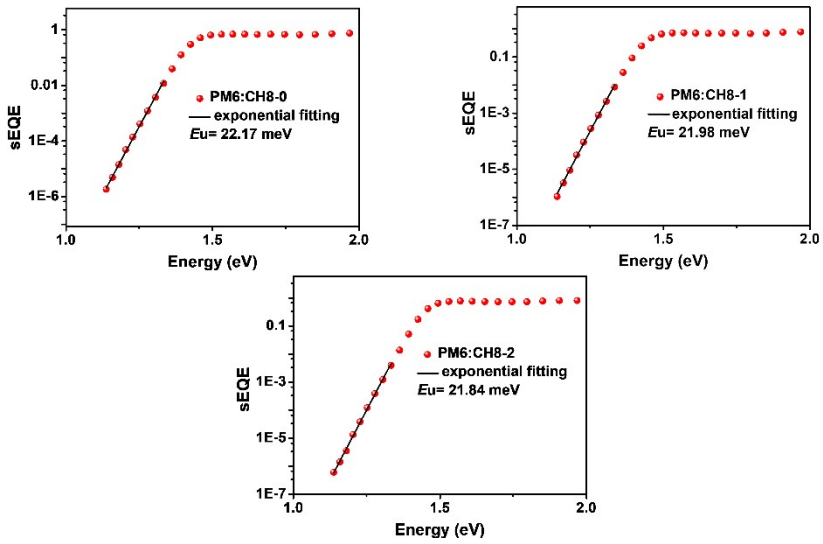

Figure S20. Sensitive external quantum efficiency spectra (sEQE), analysis of energetic disorder of optimized PM6:CH8-0, PM6:CH8-1 and PM6:CH8-2 based OSCs at the absorption onset.

3.3 Morphology analysis.

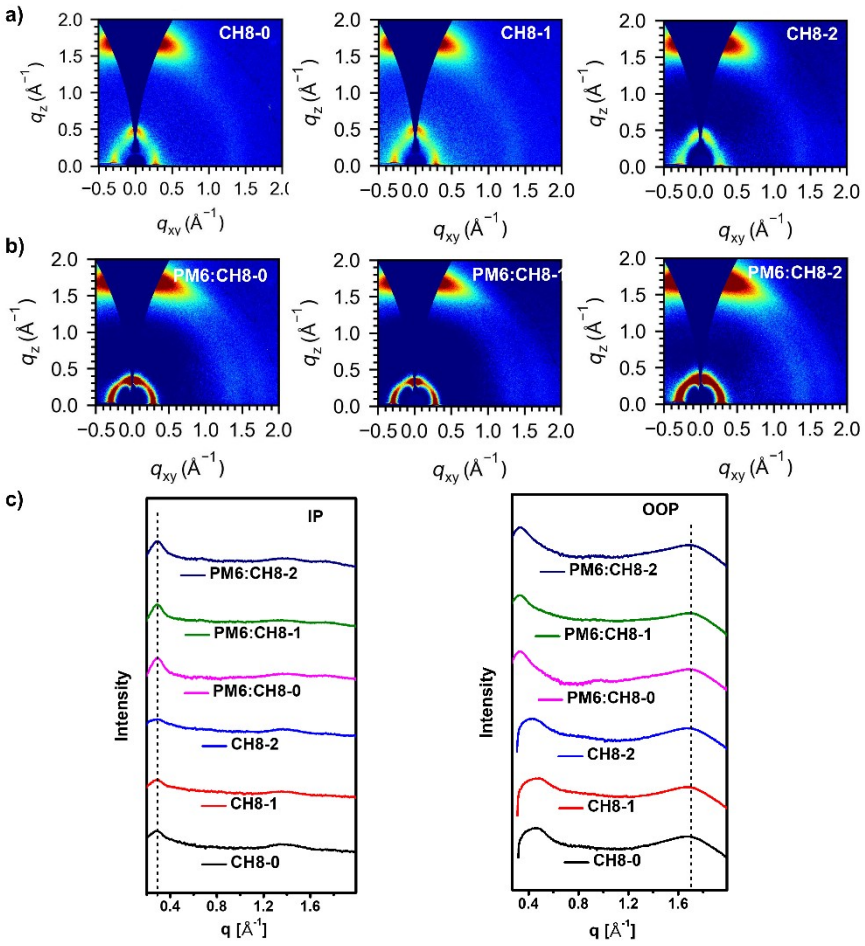

Figure S21 a) 2D GIWAXS patterns of pure films and b) blend films based on CH8-0, CH8-1 and CH8-2. c) The corresponding 1D line-cuts of CH8-0, CH8-1 and CH8-2 based neat and blend films.

Table S12. Crystal parameters extracted from GIWAXS.

Film	q(010, Å^{-1})	d-space[a] (010, Å)	CCL[b] (010, Å)	q (100, Å^{-1})	d- space[a] (100, Å)	CCL[b] (100, Å)
CH8-0	1.65	3.82	21.0	0.283	22.2	58.9
CH8-1	1.65	3.82	23.0	0.286	22.0	60.8
CH8-2	1.65	3.81	20.4	0.281	22.4	44.2
PM6:CH8-0	1.66	3.80	20.3	0.291	21.6	72.5
PM6:CH8-1	1.66	3.79	25.1	0.290	21.7	75.4
PM6:CH8-2	1.65	3.80	20.7	0.290	21.7	69.0

[a] Calculated from the equation: d-spacing = 2π/q. [b] Obtained from the Scherrer equation: CCL = 2πK/FWHM, where FWHM is the full-width at half-maximum and K is a shape factor (K = 0.9 here).

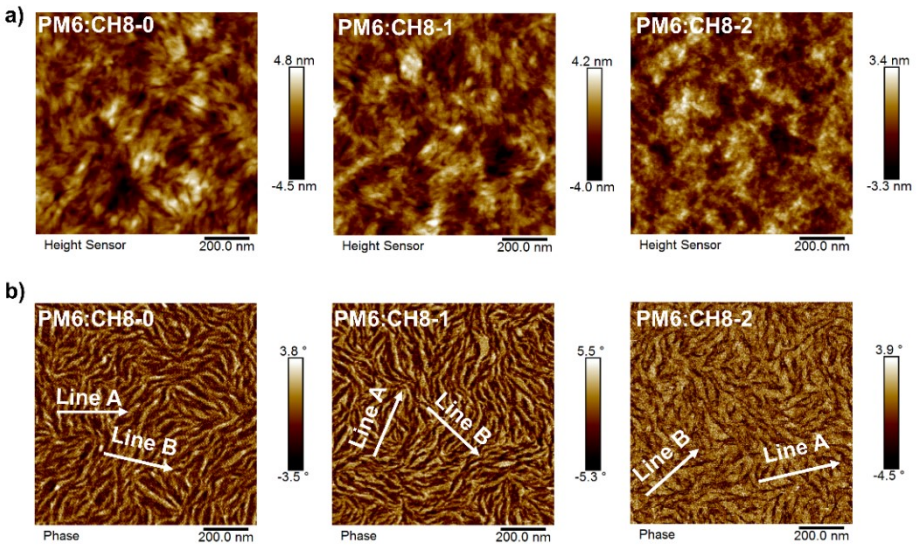

Figure S22 a) AFM height images (Root-mean square (RMS) roughness is 1.28, 1.16 and 0.94 nm for CH8-0, CH8-1 and CH8-2 based blend films, respectively) and b) phase images of CH8-0, CH8-1 and CH8-2 based blend films. The marked white arrows are to obtain the fibril width for corresponding blend films (line profiles in Figure S23).

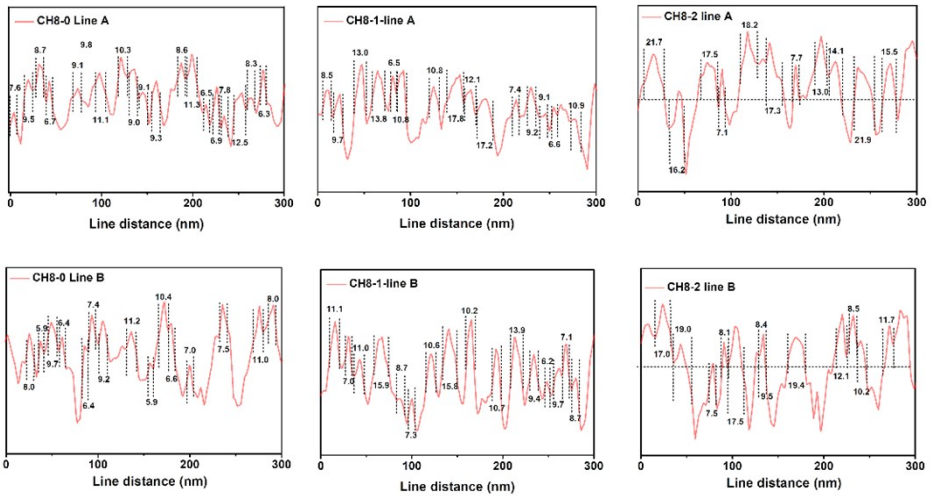

Figure S23 The line profile along the white arrows in Figure S22 to obtain the fibril width of CH8-0, CH8-1 and CH8-2 based blend films. The fibril width is obtained from the full-width at half-maximum (the distance between two adjacent dashed lines in the graph).[30]

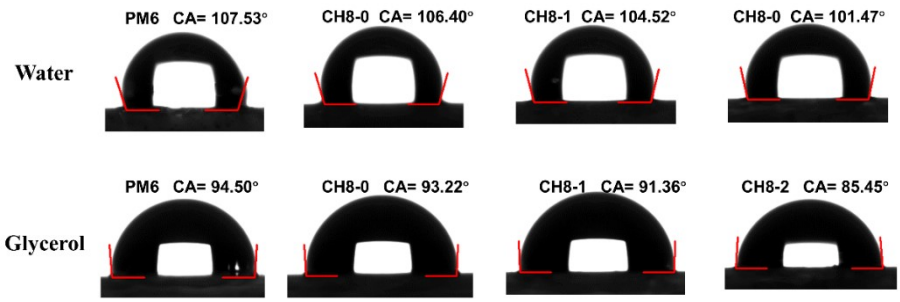

Figure S24. Contact angle images of water and glycerol droplets on the neat films of PM6, CH8-0, CH8-1 and CH8-2 films.

Table S13. Information from the top surface measured by water and glycerol contact angle.

Film	θ_{water}[°]	$\theta_{glycerol}$[°]	γ[mN m^{-1}]	$\chi_{D:A}$[a]
CH8-0 (A)	106.40	93.22	18.41	0.01
CH8-1 (A)	104.52	91.36	19.84	0.07
CH8-2 (A)	101.47	85.45	22.96	0.37
PM6 (D)	107.53	94.50	17.52	-

[a] The molecular miscibility can be evaluated by Flory–Huggins interaction parameter χ, which is calculated via using the equation of: $\chi_{D:A} \propto (\sqrt{\gamma_D} - \sqrt{\gamma_A})^2$.[31]

3.4 NMR spectra and MS.

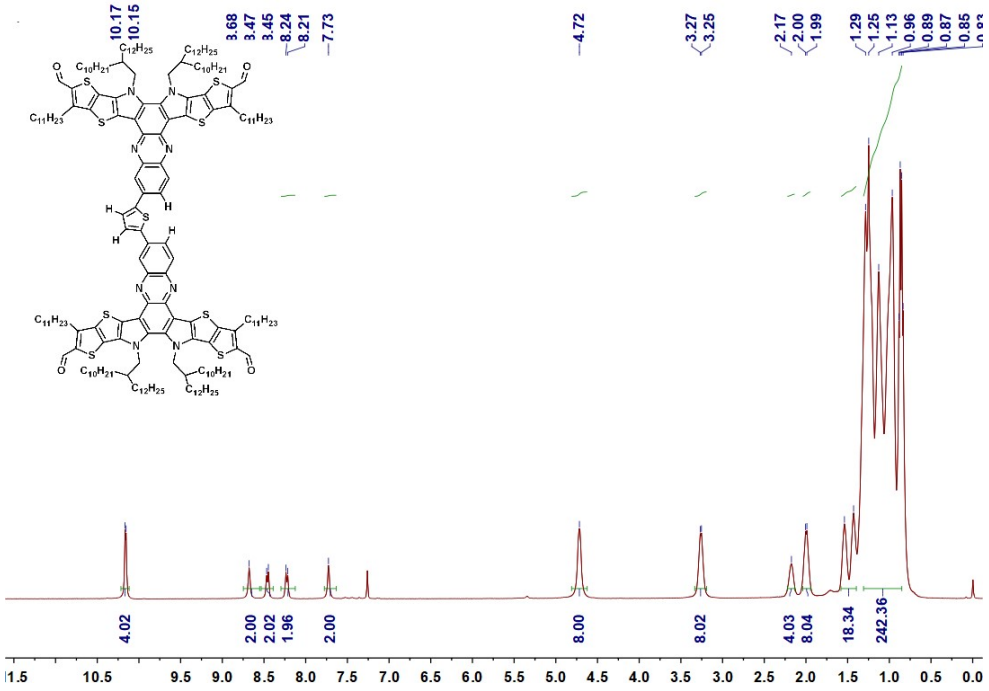

Figure S25. ^{1}H NMR spectrum of compound 2-1 at 300K in $CDCl_3$.

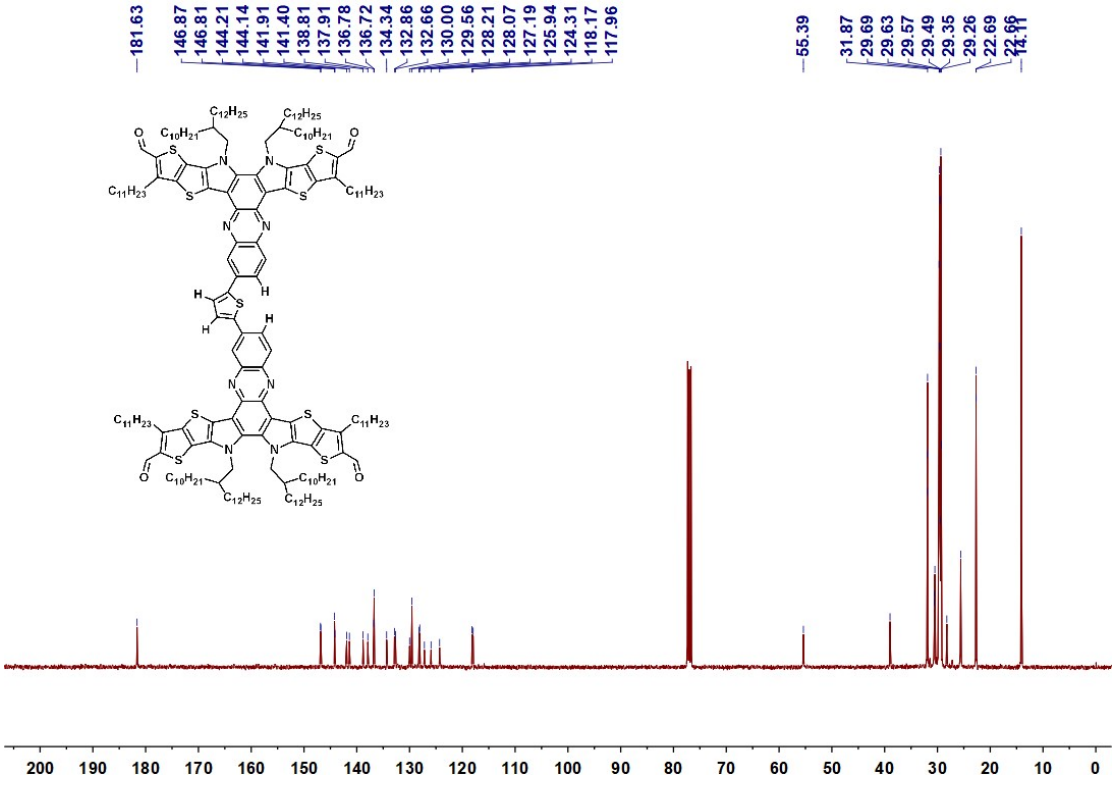

Figure S26. ^{13}C NMR spectrum of compound 2-1 at 300K in $CDCl_3$.

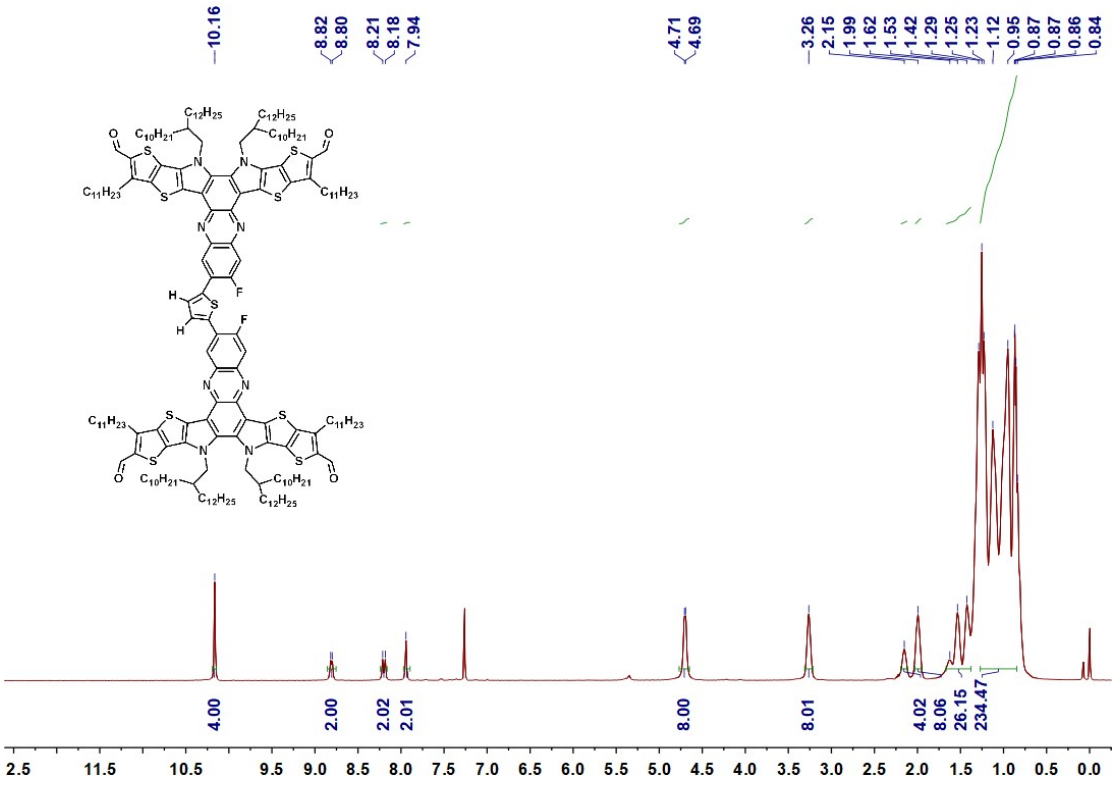

Figure S27. ^{1}H NMR spectrum of compound 2-2 at 300K in $CDCl_3$.

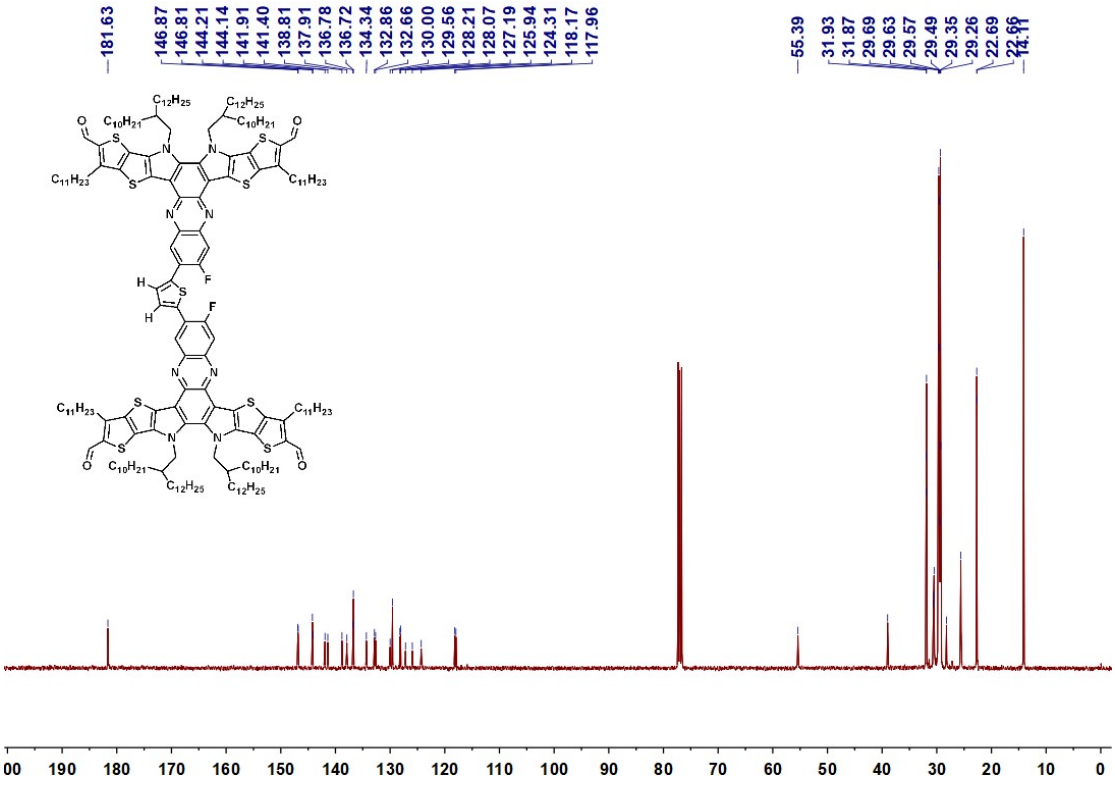

Figure S28. ^{13}C NMR spectrum of compound 2-2 at 300K in $CDCl_3$.

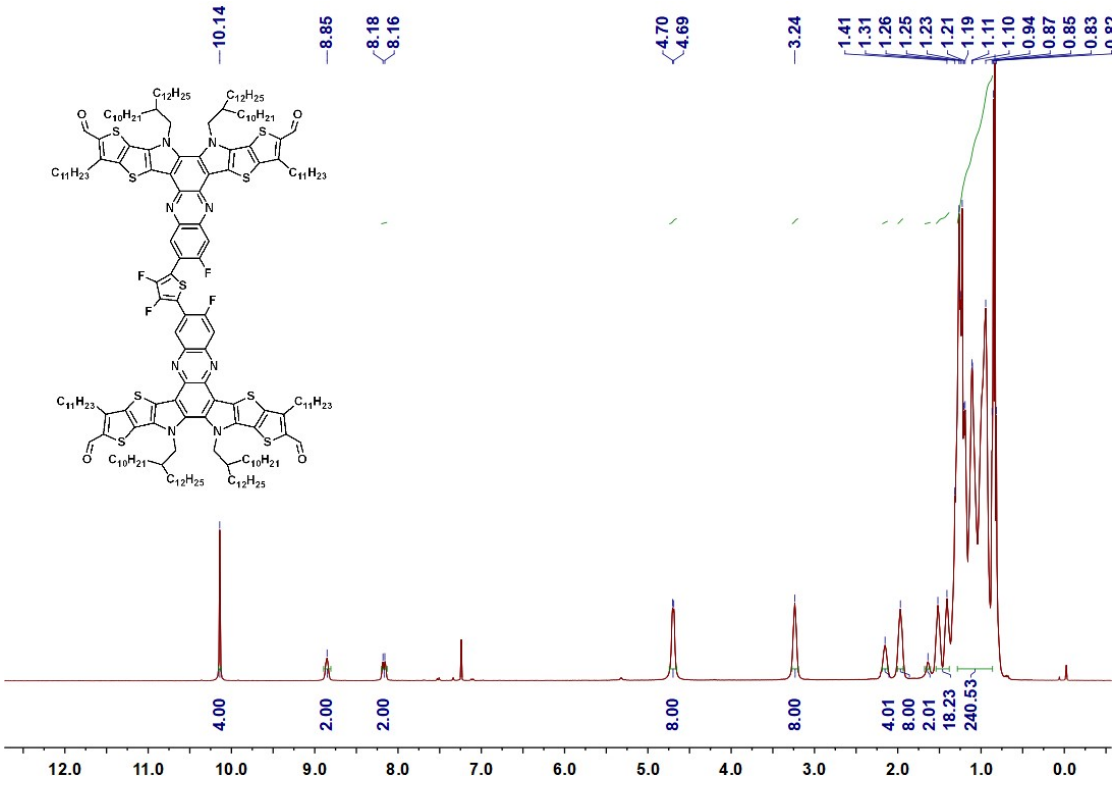

Figure S29. ^{1}H NMR spectrum of compound 2-3 at 300K in $CDCl_3$.

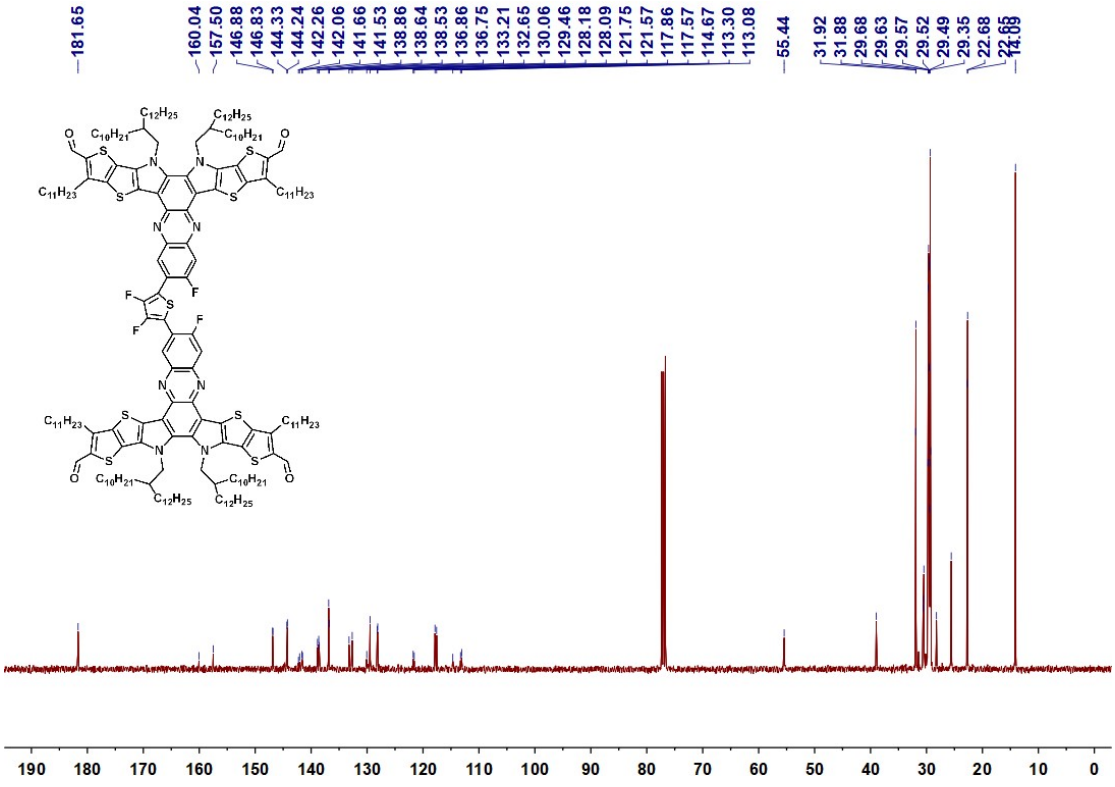

Figure S30. ^{13}C NMR spectrum of compound 2-3 at 300K in $CDCl_3$.

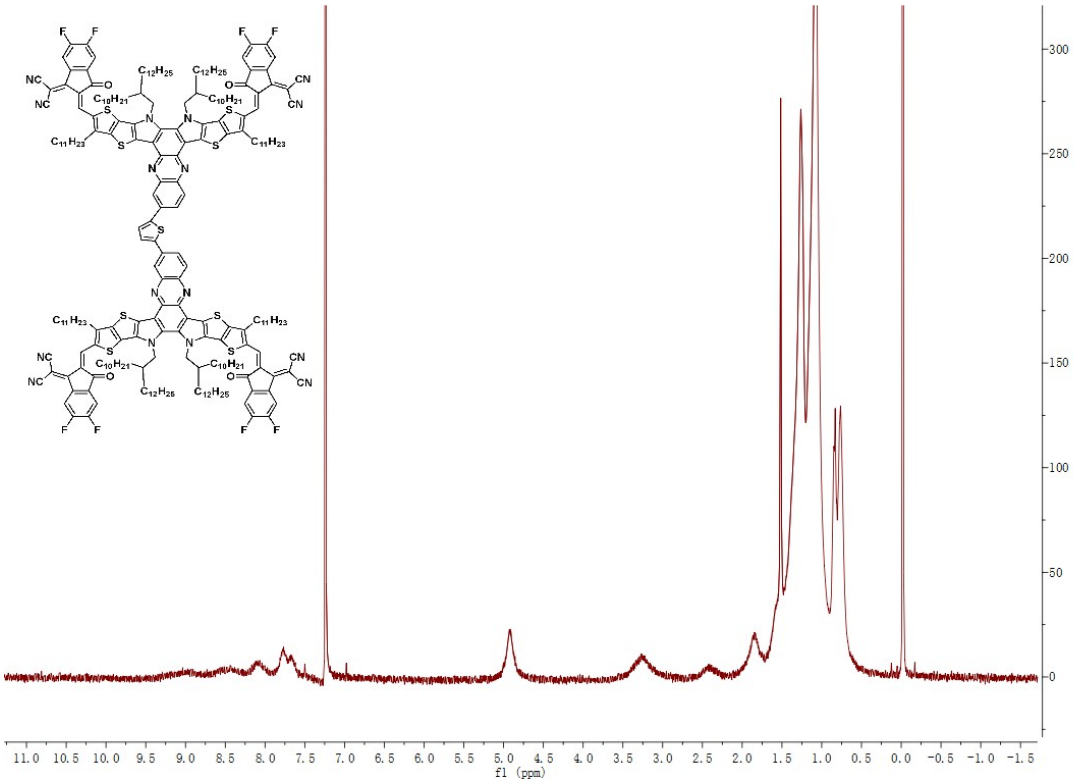

Figure S31. ^{1}H NMR spectrum of compound CH8-0 at 300K in $CDCl_3$.

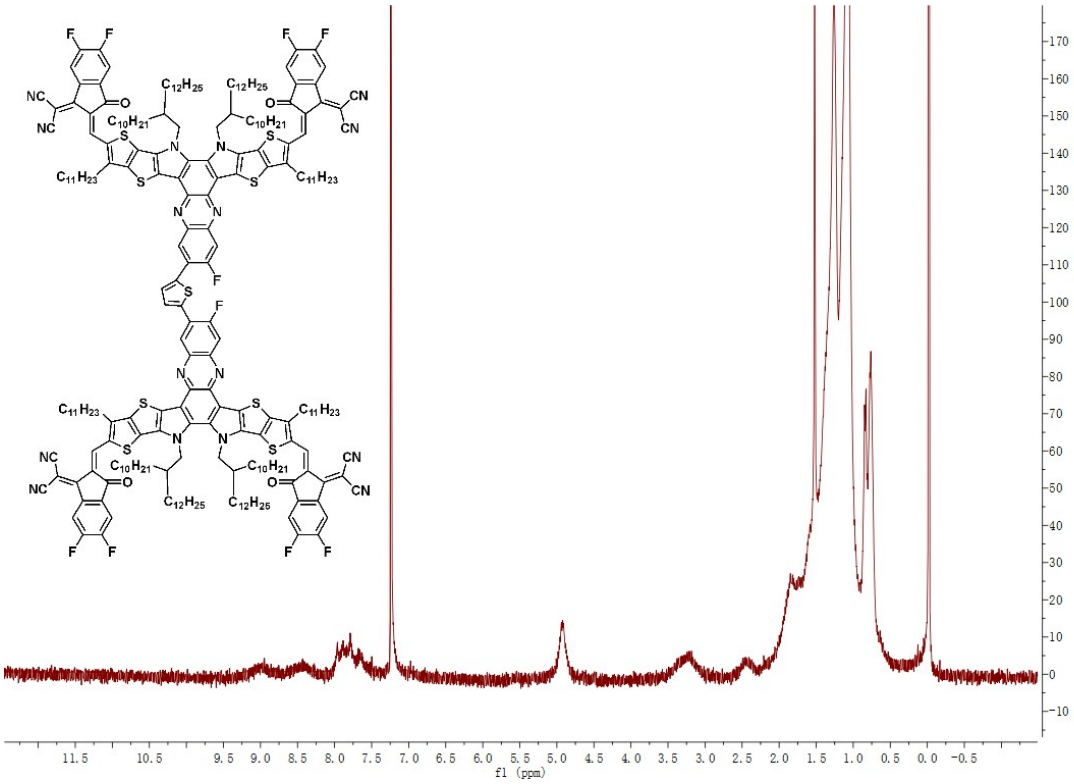

Figure S32. ^{1}H NMR spectrum of compound CH8-1 at 300K in $CDCl_3$.

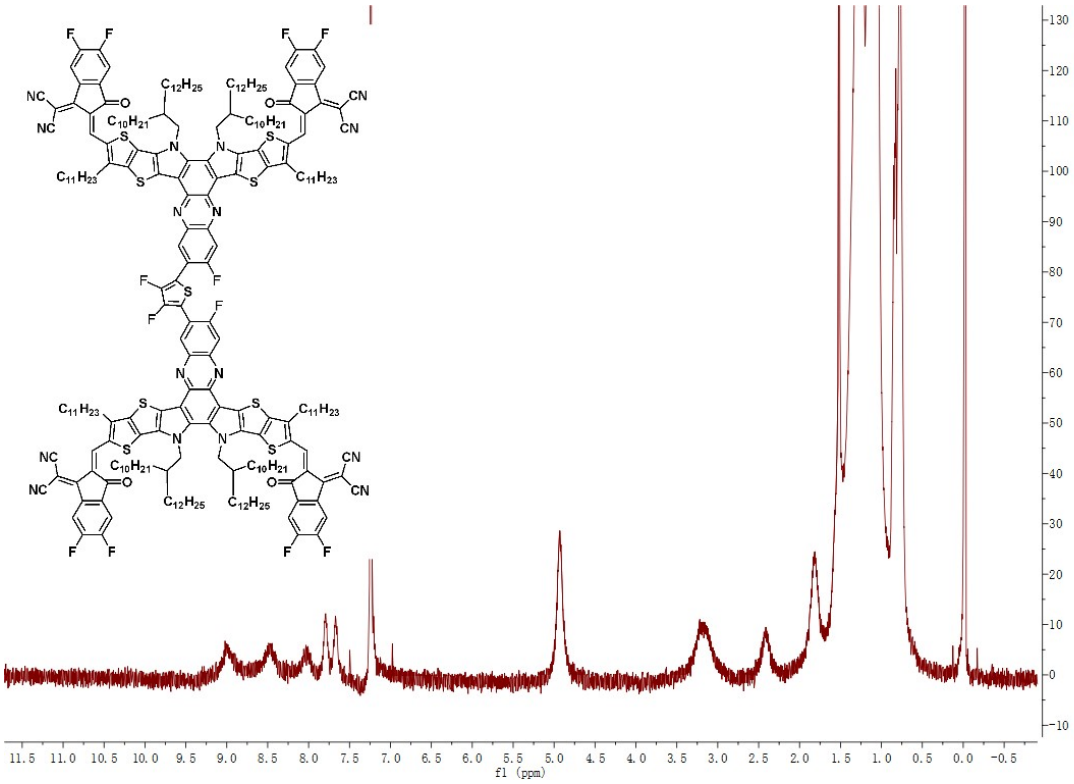

Figure S33. ^{1}H NMR spectrum of compound CH8-2 at 300K in $CDCl_3$.

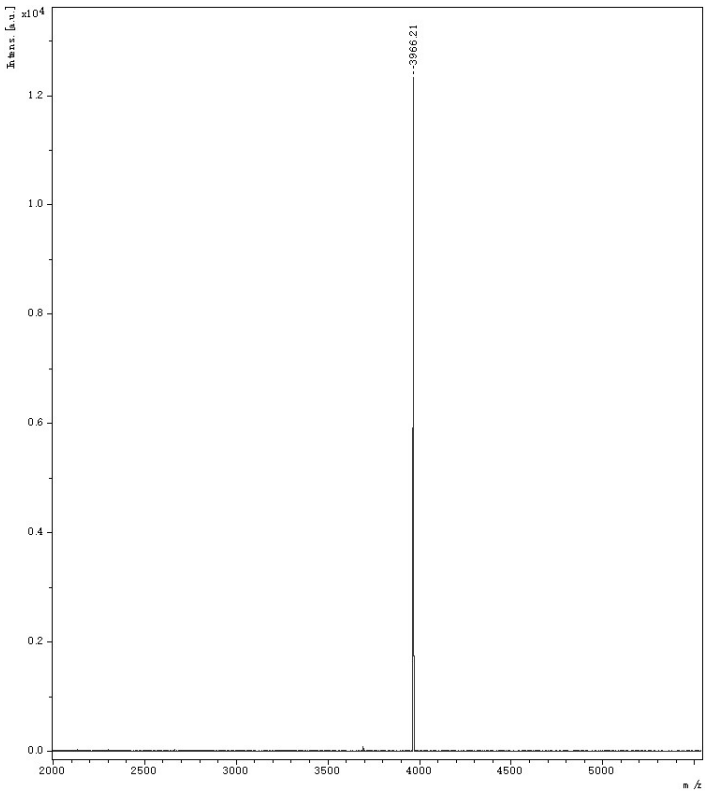

Figure 34. MS of CH8-0.

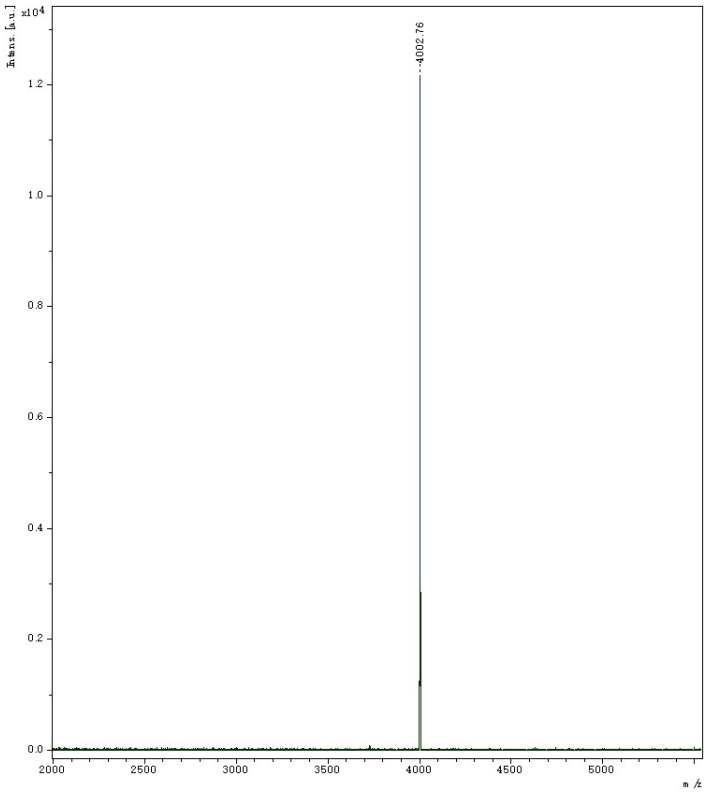

Figure 35. MS of CH8-1.

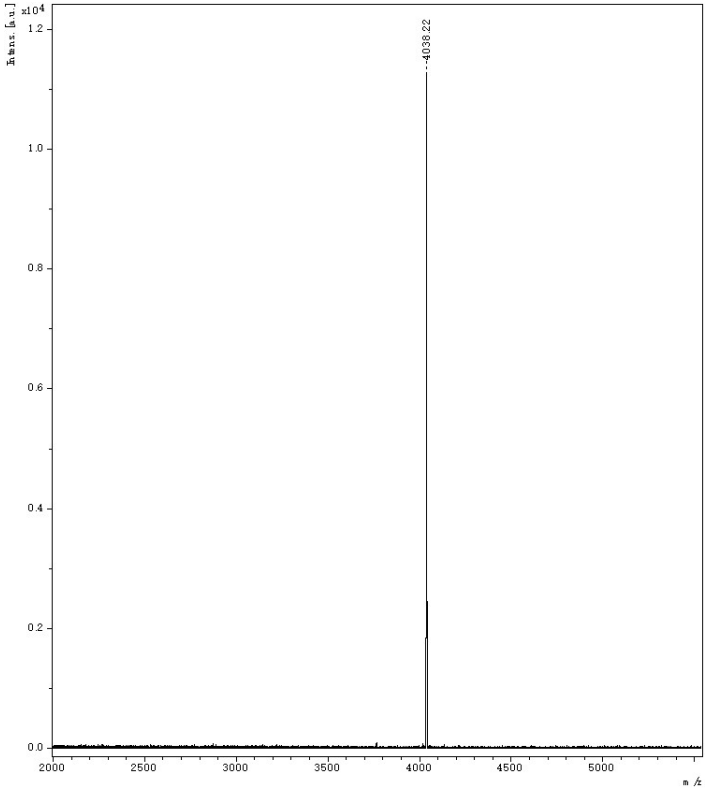

Figure 36. MS of CH8-2.

4. References.

1. H. Chen, Y. Zou, H. Liang, T. He, X. Xu, Y. Zhang, Z. Ma, J. Wang, M. Zhang, Q. Li, C. Li, G. Long, X. Wan, Z. Yao and Y. Chen, *Sci. China Chem.* **2022**, *65*, 1362-1373.
2. M. J. Frisch, et al. Gaussian 16, Gaussian, Inc.: Wallingford, CT, (2016)..
3. A. D. Becke, *J Chem Phys*, 1993, **98**, 5648-5652.
4. P. C. Hariharan and J. A. Pople, *Mol. Phys.*, 1974, **27**, 209-214.
5. X. Wan, C. Li, M. Zhang and Y. Chen, *Chem. Soc. Rev.*, 2020, **49**, 2828-2842.
6. T. Wang, W. Wang, X. Wu, H. Tong and L. Wang, *Dyes Pigm.*, 2021, **190**, 109329.
7. M. Deng, G. Zhang, L. Yu, X. Xu and Q. Peng, *Chem. Eng. J.*, 2021, **426**, 131910.
8. G. Cai, Y. Li, J. Zhou, P. Xue, K. Liu, J. Wang, Z. Xie, G. Li, X. Zhan and X. Lu, *ACS Appl. Mater. Interfaces*, 2020, **12**, 50660-50667.
9. M. Wu, J.-P. Yi, L. Chen, G. He, F. Chen, M. Y. Sfeir and J. Xia, *ACS Appl. Mater. Interfaces*, 2018, **10**, 27894-27901.
10. X. Wu, W. Wang, H. Hang, H. Li, Y. Chen, Q. Xu, H. Tong and L. Wang, *ACS Appl. Mater. Interfaces*, 2019, **11**, 28115-28124.
11. K. Wang, P. Xia, K. Wang, X. You, M. Wu, H. Huang, D. Wu and J. Xia, *ACS Appl. Mater. Interfaces*, 2020, **12**, 9528-9536.
12. G. Cai, W. Wang, J. Zhou, Y. Xiao, K. Liu, Z. Xie, X. Lu, J. Lian, P. Zeng, Y. Wang and X. Zhan, *ACS Materials Letters*, 2019, **1**, 367-374.
13. W. Wu, G. Zhang, X. Xu, S. Wang, Y. Li and Q. Peng, *Adv. Funct. Mater.*, 2018, **28**, 1707493.
14. Y.-J. Hwang, H. Li, B. A. E. Courtright, S. Subramaniyan and S. A. Jenekhe, *Adv. Mater.*, 2016, **28**, 124-131.
15. Y. Duan, X. Xu, H. Yan, W. Wu, Z. Li and Q. Peng, *Adv. Mater.*, 2017, **29**, 1605115.
16. X. Xu, G. Zhang, L. Yu, R. Li and Q. Peng, *Adv. Mater.*, 2019, **31**, 1906045.
17. X. Meng, M. Li, K. Jin, L. Zhang, J. Sun, W. Zhang, C. Yi, J. Yang, F. Hao, G.-W. Wang, Z. Xiao and L. Ding, *Angew. Chem. Int. Ed.*, 2022, **61**, e202207762.
18. M. Wu, J.-P. Yi, J. Hu, P. Xia, H. Wang, F. Chen, D. Wu and J. Xia, *J. Mater. Chem. C*, 2019, **7**, 9564-9572.
19. S. Chen, D. Meng, J. Huang, N. Liang, Y. Li, F. Liu, H. Yan and Z. Wang, *CCS Chemistry*, 2021, **3**, 78-84.
20. D. Liu, T. Wang, Z. Chang, N. Zheng, Z. Xie and Y. Liu, *J. Mater. Chem. A*, 2021, **9**, 2319-2324.
21. D. Meng, H. Fu, C. Xiao, X. Meng, T. Winands, W. Ma, W. Wei, B. Fan, L. Huo, N. L. Doltsinis, Y. Li, Y. Sun and Z. Wang, *J. Am. Chem. Soc.*, 2016, **138**, 10184-10190.
22. J. Zhang, Y. Li, J. Huang, H. Hu, G. Zhang, T. Ma, P. C. Y. Chow, H. Ade, D. Pan and H. Yan, *J. Am. Chem. Soc.*, 2017, **139**, 16092-16095.
23. Z. Ma, T. Winands, N. Liang, D. Meng, W. Jiang, N. L. Doltsinis and Z. Wang, *Sci. China Chem.*, 2020, **63**, 208-214.
24. H. Chen, X. Cao, X. Xu, C. Li, X. Wan, Z. Yao and Y. Chen, *Chin. J. Polym. Sci.*, 2022, **40**, 921-927.
25. Y. Zou, H. Chen, X. Bi, X. Xu, H. Wang, M. Lin, Z. Ma, M. Zhang, C. Li, X. Wan, G. Long, Y. Zhaoyang and Y. Chen, *Energy Environ. Sci.*, 2022, **15**, 3519-3533.
26. S. M. Swick, J. M. Alzola, V. K. Sangwan, S. H. Amsterdam, W. Zhu, L. O. Jones, N. Powers-Riggs, A. Facchetti, K. L. Kohlstedt, G. C. Schatz, M. C. Hersam, M. R. Wasielewski and T. J. Marks, *Adv. Energy Mater.*, 2020, **10**, 2000635.

27. G. Li, X. Zhang, L. O. Jones, J. M. Alzola, S. Mukherjee, L.-w. Feng, W. Zhu, C. L. Stern, W. Huang, J. Yu, V. K. Sangwan, D. M. DeLongchamp, K. L. Kohlstedt, M. R. Wasielewski, M. C. Hersam, G. C. Schatz, A. Facchetti and T. J. Marks, *J. Am. Chem. Soc.*, 2021, **143**, 6123-6139.
28. Y. Wang, D. Qian, Y. Cui, H. Zhang, J. Hou, K. Vandewal, T. Kirchartz and F. Gao, *Adv. Energy Mater.*, 2018, **8**, 1801352.
29. J. Liu, S. Chen, D. Qian, B. Gautam, G. Yang, J. Zhao, J. Bergqvist, F. Zhang, W. Ma, H. Ade, O. Inganäs, K. Gundogdu, F. Gao and H. Yan, *Nat. Energy*, 2016, **1**, 16089.
30. L. Zhu, M. Zhang, J. Xu, C. Li, J. Yan, G. Zhou, W. Zhong, T. Hao, J. Song, X. Xue, Z. Zhou, R. Zeng, H. Zhu, C.-C. Chen, R. C. I. MacKenzie, Y. Zou, J. Nelson, Y. Zhang, Y. Sun and F. Liu, *Nat. Mater.*, 2022, **21**, 656-663.
31. S. Nilsson, A. Bernasik, A. Budkowski and E. Moons, *Macromolecules*, 2007, **40**, 8291-8301.